nature astronomy

Article

https://doi.org/10.1038/s41550-023-02153-z

A link between repeating and non-repeating fast radio bursts through their energy distributions

Received: 17 January 2023

Accepted: 30 October 2023

Published online: 4 January 2024

Check for updates

F. Kirsten[1,2] ✉, O. S. Ould-Boukattine[2,3], W. Herrmann[4], M. P. Gawroński[5], J. W. T. Hessels[2,3], W. Lu[6], M. P. Snelders[2,3], P. Chawla[3], J. Yang[1], R. Blaauw[2], K. Nimmo[7], W. Puchalska[5], P. Wolak[5] & R. van Ruiten[3]

Fast radio bursts (FRBs) are extremely energetic, millisecond-duration radio flashes that reach Earth from extragalactic distances. Broadly speaking, FRBs can be classified as repeating or (apparently) non-repeating. It is still unclear, however, whether the two types share a common physical origin and differ only in their activity rate. Here we report on an observing campaign that targeted one hyperactive repeating source, FRB 20201124A, for more than 2,000 h using four 25–32 m class radio telescopes. We detected 46 high-energy bursts, many more than one would expect given previous observations of lower-energy bursts using larger radio telescopes. We find a high-energy burst distribution that resembles that of the non-repeating FRB population, suggesting that apparently non-repeating FRB sources may simply be the rarest bursts from repeating sources. Also, we discuss how FRB 20201124A contributes strongly to the all-sky FRB rate and how similar sources would be observable even at very high redshift.

The vast majority of fast radio burst (FRB) sources have been detected only once[1], but a small subpopulation (~2.6%) is known to burst repeatedly[2,3]. Nonetheless, many apparent non-repeaters may be capable of repeating. In particular, recent results have shown that there is a wide range of FRB activity levels, with only very few sources being highly active[3]. This suggests that the apparent non-repeaters are simply the least active FRB sources. However, statistical studies have shown that the average emission bandwidth and burst duration differ between repeaters and non-repeaters[1,4]. This suggests that repeaters and non-repeaters have different origins, either a physically distinct progenitor or that a single type of source can produce different types of bursts.

Probing the burst energy distribution of FRBs across many orders of magnitude, for both individual sources and the entire population, could help determine whether repeaters and non-repeaters have the same burst engines.

Typically, FRBs have isotropic-equivalent burst energies E in the range[5] $E \approx 10^{36-41}$ erg, though burst energies as high as $E = 2 \times 10^{42}$ erg have been reported for distant sources[6]. Telescope sensitivity strongly limits our ability to detect weaker bursts and on-sky time limits our ability to detect the rarest, most energetic bursts. In this Article, we will consider the spectral energy density $E_\nu = E/\nu$, where ν is the observed bandwidth of the emission. To convert energies quoted in the literature to spectral energies, we adopt a fiducial bandwidth of 300 MHz (unless specified otherwise) as a 'middle ground' between the statistically different bandwidths of repeating and apparently non-repeating FRBs[4].

The cumulative burst spectral energy distribution of repeating FRBs can be modelled by a single or broken power law[7,8], $R(>E_\nu) \propto E_\nu^{\gamma}$,

[1]Department of Space, Earth and Environment, Chalmers University of Technology, Onsala Space Observatory, Onsala, Sweden. [2]ASTRON, Netherlands Institute for Radio Astronomy, Dwingeloo, the Netherlands. [3]Anton Pannekoek Institute for Astronomy, University of Amsterdam, Amsterdam, the Netherlands. [4]Astropeiler Stockert e.V., Bad Münstereifel, Germany. [5]Institute of Astronomy, Faculty of Physics, Astronomy and Informatics, Nicolaus Copernicus University, Toruń, Poland. [6]Department of Astronomy and Theoretical Astrophysics Center, UC Berkeley, Berkeley, CA, USA. [7]MIT Kavli Institute for Astrophysics and Space Research, Massachusetts Institute of Technology, Cambridge, MA, USA. ✉e-mail: franz.kirsten@chalmers.se

https://doi.org/10.1038/s41550-023-02153-z

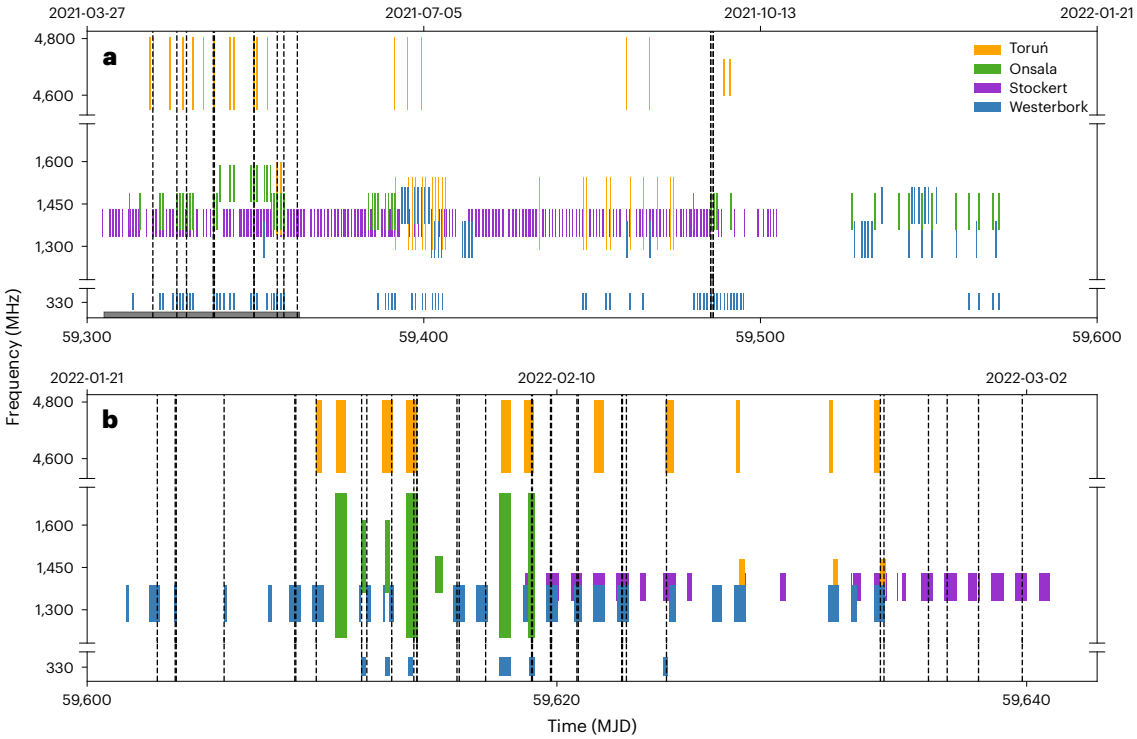

Fig. 1 | Overview of the FRB 20201124A monitoring campaign. a, MJD range 59,300–59,600. **b**, MJD 59,600–59,645. The corresponding calendar dates are listed on the top *x* axes. Each coloured vertical block indicates an observation and associated telescope (annotated in the figure legend). The placement and extent along the *y* axes indicate the observing band. Note that the frequency axis is discontinuous. The vertical black dashed lines denote detections of bursts from FRB 20201124A in the frequency range 1,202–1,714 MHz (despite spanning the entire frequency axis for visualization purposes). The horizontal grey bar along the bottom of **a** highlights the time range overlapping the FAST observations[20] discussed in the text.

with the slope γ sometimes steepening towards the high-energy tail, reaching values as extreme as $\gamma = -4.9$ (ref. 9). The measured value of γ varies between sources and between observing epochs. For example, for FRB 20121102A, γ ranges[10,11] between −0.61 and −1.8. There is also a hint that the burst energy distribution of FRB 20121102A flattens[10,11] at the highest spectral energies ($E_\nu \gtrsim 3 \times 10^{31}$ erg Hz^{-1}), although the low number of observed events precludes a robust conclusion.

In contrast, for apparently non-repeating FRBs, modelling of the population[12–14] shows a much flatter energy distribution, with γ between about 0 and −1. Hyperactive repeating sources provide an opportunity to probe the high-energy burst distribution and compare it with that of apparently non-repeating sources. This is an important way to investigate whether repeaters and non-repeaters have the same progenitors. It also provides key input for FRB population simulations and applications for probing cosmology because the highest-achievable burst energies directly relate to the maximum distances from which we can observe FRBs.

One of the most hyperactive FRB sources to date is FRB 20201124A (ref. 15), with >3,000 bursts detected in ~25 h of observations with the FAST telescope[16]. In addition, the source has been reported to emit high-fluence bursts[17] that are detectable with relatively small 25–32 m class radio telescopes. FRB 20201124A is in a region of enhanced star formation[18] in a massive star-forming galaxy at redshift[19] $z = 0.098$. The known distance allows us to infer burst energies from measured fluences.

Observations and results

We observed FRB 20201124A between modified Julian date (MJD) 59,309 and MJD 59,641 (April 2021 to March 2022; Fig. 1) for 2,281 h, spread over a 1-year time span. Four radio telescopes were used: the 25 m dish in Onsala, Sweden (O8); RT1, a 25 m dish in Westerbork, the Netherlands (Wb); the 32 m dish in Toruń, Poland (Tr); and the 25 m telescope in Stockert, Germany (St). The observations were coordinated between the four telescopes with the aim of covering as broad a radio-frequency bandwidth as possible during contemporaneous observations while increasing the overall time on source (Table 1). During times of high source activity, we observed for up to 12 h daily over the course of several weeks. We recorded raw voltages (amplitude and phase data) at Wb, O8 and Tr, whereas St recorded total-intensity data (Methods). The data were processed and searched for bursts using standard techniques and tools (Methods).

We detected 46 unique bursts in the frequency range 1,200–1,750 MHz (L-band), after accounting for events that were detected by several telescopes simultaneously (Table 2). We consider subcomponents to be part of a single burst if they are separated by no more than 100 ms from each other. This choice is driven by the observed wait-time distribution[8,20] of FRB 20201124A. Among our detections is the highest-fluence burst ever detected from this source (fluence $F \approx 1{,}600$ Jy ms; Fig. 2). Fourteen bursts were detected simultaneously at more than one dish. No bursts were discovered at P-band (300–364 MHz) or at C-band (4,550–4,806 MHz), and none of the bursts discovered at L-band had a counterpart in the other frequency bands (Methods and Extended Data Table 1). During our campaign, Apertif[21] reported the detection of two bursts from FRB 20201124A, one of which we detected as well (B23-wb), whereas the other occurred when Wb was observing at P-band. The dynamic spectra, time series and spectra for a subset of bursts are shown in Fig. 2 (the full set is shown in Extended Data Figs. 1–3). Almost half of the bursts (18/46) were composed of two or more components, most of which (13/18, that is ~70%) show the canonical 'sad trombone' effect[22] in which burst emission at lower frequencies arrives later in time, even after correcting for the dispersive delay. We used the structure-optimizing code DM-phase[23] on one of our brightest multi-component bursts (B13-o8; Fig. 2) to obtain a dispersion measure DM = 410.8 ± 0.3 pc cm^{-3} (Methods and Extended Data

Table 1 | Observational set-up

Station	Band	Frequency (MHz)	Bandwidth[a] (MHz)	Bandwidth per sub-band (MHz)	SEFD[b] (Jy)	Completeness[c] (Jyms)	Time observed (h)
Wb	P	300–364	60	8	2100	91	649.51
Wb	$L_{Wb\text{-}1}$	1,259–1,387	100	16	420	14	383.1
Wb	$L_{Wb\text{-}2}$	1,382–1,510	100	16	420	14	129.5
St	L_{St}	1,332.5–1,430.5	98	98	1,100/385	39/14	1,431.7
O8	$L_{O8\text{-}1}$	1,360–1,488	100	16	310	10	415.7
O8	$L_{O8\text{-}2}$	1,460–1,588	100	16	310	10	85.7
O8	$L_{O8\text{-}3}$	1,360–1,616	200	16	310	7	9.8
O8	$L_{O8\text{-}4}$	1,202–1,714	350	32	310	5	40.9
Tr	$L_{Tr\text{-}1}$	1,290–1,546	200	32	350	8	116.9
Tr	$L_{Tr\text{-}2}$	1,340–1,596	200	32	350	8	22.4
Tr	$L_{Tr\text{-}3}$	1,350–1,478	100	16	350	12	15.6
Tr	$C_{Tr\text{-}1}$	4,550–4,806	240	32	220	5	227.7
Tr	$C_{Tr\text{-}2}$	4,600–4,728	120	32	220	7	16.4
Total telescope time/total time on source (h)[d]							3,545/2,281

[a]Effective bandwidth accounting for RFI and band edges. [b]From the EVN status page (with the exception of St, for which the two values indicate the pre- and post-upgrade sensitivity). [c]Assuming a 15σ detection threshold and a pulse width of 1 ms. [d]Total time on source accounts for the overlap between the participating stations.

Table 2). This DM is used throughout the rest of the analysis for all bursts. The burst properties listed in Extended Data Table 3 were obtained from incoherently dedispersed data, except for the time of arrival (TOA), which was measured using coherently dedispersed data products when baseband data were available, that is, for all bursts detected by Tr, Wb and O8. For the St bursts, incoherently dedispersed data products were used for the TOAs (Methods). Particular care was given to the computation of the burst fluences because the large brightness and strong scintillation of the bursts systematically affects the recorded data through saturation effects (Methods and Extended Data Figs. 4 and 5). The median scintillation bandwidth ν_s, scaled to a canonical observing frequency of 1 GHz, $\nu_s^{1\mathrm{GHz}} = 0.4 \pm 0.1$ MHz, is consistent with previous observations[24]. Furthermore, we measured the characteristic temporal separation between individual burst components to be $\delta t = 4.1^{+4.4}_{-2.1}$ ms (Extended Data Fig. 6). This value is a factor 2–10 larger than the one reported[22] for FRB 20121102A.

The vast majority of bursts were detected during two time ranges, lasting roughly 60 and 40 d each (Fig. 1 and Extended Data Table 3). Figure 3a shows the distributions of the burst spectral energy densities E_ν during the first activity window compared with those observed with FAST during the same time range[20] (MJD 59,305–59,363). The energy distribution of our bursts shows no break, so we fitted a simple power law to the cumulative burst rate as a function of spectral energy density, $R(>E_\nu) \propto E_\nu^\gamma$, using a least-squares technique (Methods). Jointly fitting the O8 and St data yields a power-law index $\gamma = -0.48 \pm 0.11 \pm 0.03$ (where the first error is the formal fitting uncertainty and the second error is derived from bootstrapping; Methods). This value is a factor 3 lower (flatter) than that observed by FAST[20] for $E_\nu > 5.9 \times 10^{29}$ erg Hz^{-1} (Methods), where $\gamma_2 = -1.5 \pm 0.1 \pm 0.1$. The value of γ_2 was derived by fitting a broken power law to the data split into energy bins[20], an approach that is not applicable for the relatively low number of bursts we detected. Therefore, for better comparability, we refitted the FAST data following our technique (Methods) to find $\gamma_{\mathrm{FAST}} = -1.947 \pm 0.011 \pm 0.063$, which agrees with γ_2 within 2σ. The bursts and the associated cumulative burst rates that we detected with O8, Wb and St during the second activity window after MJD 59,602 are shown in Fig. 3b. We fitted the data from Wb and St in the same way as described above and found power-law slopes $\gamma_{\mathrm{St}} = -1.43 \pm 0.09 \pm 0.41$ and $\gamma_{\mathrm{Wb}} = -0.85 \pm 0.05 \pm 0.09$ for the St and Wb bursts, respectively. These energy distribution slopes are steeper than that from the first activity window but are still much flatter for the Wb data than that of the high-energy tail in the FAST data[20]. The slope of the St data during this epoch agrees with the one from Wb within the summed 1σ uncertainties but also agrees with γ_2 from ref. 20. Since the sensitivity thresholds of O8, Wb and St during the second activity window are comparable, we combined the data from all three telescopes from both activity windows (excluding the data from St during the first window as its detection threshold was a factor ~3 higher at that time; Methods) to get an estimate of the average slope γ_{av} of the energy distribution around an observing frequency of 1.3 GHz. Fitting the combined data yields $\gamma_{\mathrm{av}} = -1.09 \pm 0.03 \pm 0.06$ (Fig. 4).

Table 2 | Observing hours and number of bursts detected per active period and dish

	Epoch 1[a]		Epoch 2[b]	
Station	Hours[c]	N[d]	Hours[c]	N[d]
Wb	9	0	199	24
O8	257	8	58	6
Tr	22	1	16	1
St	390	3	178	13

[a]MJD 59,305–59,363. [b]MJD 59,602–59,642. [c]Hours spent on source at L-band. [d]Number of bursts detected.

Discussion

Lensing cannot explain FRB 20201124A's high-energy bursts

The highest-energy bursts ($E_\nu \gtrsim 10^{31}$ erg Hz^{-1}) observed from FRB 20201124A occurred at a much higher rate than expected based on the energy distribution of lower-energy bursts. One possible explanation is that burst brightness is boosted by propagation effects, such as lensing in an inhomogeneous plasma[25] local to FRB 20201124A or an intervening gravitational potential[26]. However, if all bursts were affected equally by such a lens, the energy distribution would be shifted as a whole and no difference between the power-law slopes of low- and high-energy bursts would be seen. Moreover, in the limit of strong magnification with magnification factor $\mu \gg 1$, the lensing cross

https://doi.org/10.1038/s41550-023-02153-z

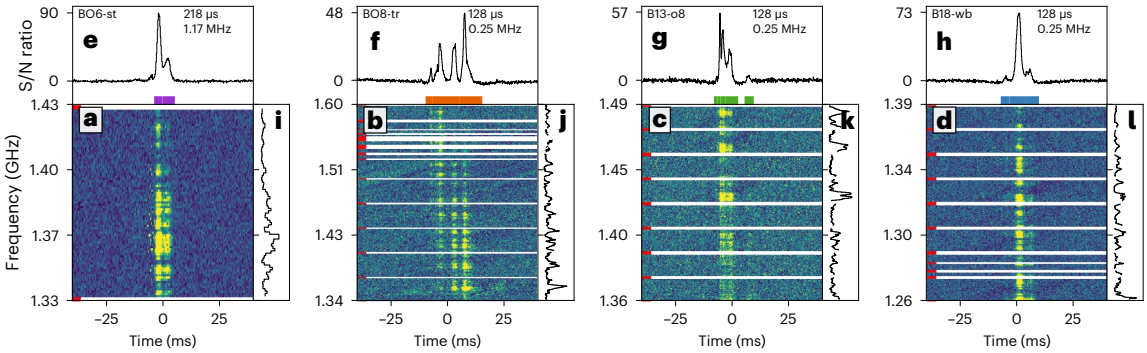

Fig. 2 | Subset of bursts detected in this campaign. a–d, Dedispersed dynamic spectra for St (**a**), Tr (**b**), O8 (**c**) and Wb (**d**). For Tr, O8 and Wb, the spectra were coherently dedispersed using SFXC, whereas the spectrum for St was incoherently dedispersed with DSPSR as no baseband data were available. The horizontal white lines with the red marker on the left denote the frequency ranges that were flagged because of RFI. For visualization, the data were capped at the 98th percentile. **e–h**, Frequency-averaged time series for St (**e**), Tr (**f**), O8 (**g**) and Wb (**h**). The pulse ID is given in the top left corner. The time and frequency resolutions used for the plots are given in the top right corner. **i-l**, Spectra of the time-averaged 'on-time' of the pulses for St (**i**), Tr (**j**), O8 (**k**) and Wb (**l**). This on-time is indicated by the coloured horizontal bar under each time series. The colour encodes the telescope at which the pulse was detected: purple for St, orange for Tr, green for O8 and blue for Wb. The same on-time was used to compute the fluences in Extended Data Table 3. The full set of bursts is shown in Extended Data Figs. 1–3.

section $\sigma(\mu) \propto \mu^{-2}$ would be independent of the lensing potential[26,27]. Thus, if the brightest bursts that we see were caused by lensing, we would expect $\gamma \approx -2$, which is inconsistent with our measurements. If the amplification due to plasma lensing has a temporal dependence[28], one would expect a burst rate distribution that is variable in time. However, as shown in Fig. 1, we detected high-energy bursts throughout the entirety of the time range that was covered by FAST, and there is no evidence for a variable energy distribution within the time range MJD 59,305–59,363. Thus, we conclude that the flattening of the burst energy distribution at high energies is most probably not a propagation effect. Rather, it more probably indicates that there is a difference in the emission mechanism, emission site or beaming angle between low- and high-energy bursts.

FRB 20201124A as a link between repeaters and non-repeaters

Burst rates as a function of energy have been reported for several repeating FRB sources, with the measured slopes of the fitted power-law distribution ranging from as steep as −4.9 (ref. 9) to as flat as −0.5 (ref. 11). The slopes vary both as a function of time and as a function of the energy range that is considered. In general, the slope is apparently flatter towards lower energies[11,20] ($E_\nu \lesssim 10^{29}$ erg Hz^{-1}). However, this can often be attributed to a lower completeness near the detection threshold of the telescope that is measuring the bursts. Nonetheless, in some cases, the low-energy turnover appears to be intrinsic to the emission process[7,8,20]. The slope usually steepens towards the high-energy end ($E_\nu \gtrsim 3 \times 10^{29}$ erg Hz^{-1}) of the distribution[8], but a slight gradual flattening of the burst rates for very high-energy bursts ($E_\nu \gtrsim 10^{31}$ erg Hz^{-1}) has been observed for at least one source[10,11]. Here we observe a strong flattening of the burst rate slope in a previously unexplored ultra-high-energy range for FRB 20201124A.

Unaffected by the limited bandwidth of our observations (Methods), the average high-energy slope that we measure (Fig. 4) broadly agrees with that found for non-repeating FRBs[14], and our value also agrees with various empirical models[12,13] that find a power-law slope $\gamma \approx -1$ for non-repeating FRBs. This indicates that the distribution of the ultra-high-energy tail ($E_\nu \gtrsim 10^{31}$ erg Hz^{-1}) of FRB 20201124A bursts resembles that of non-repeaters, whereas the low-energy bulk of the bursts does not. Thus, we are seeing both repeater- and non-repeater-like behaviour from a single FRB source.

For apparently non-repeating FRBs, we may be observing bursts from a similar high-energy tail as what we report here for FRB 20201124A. As such bursts are extremely rare, occurring once per hundreds to thousands of hours or more (we see no high-energy cutoff in the burst energy distribution), such a source would appear to be non-repeating.

However, the low- and high-energy ends of the burst distribution for FRB 20201124A are currently statistically indistinguishable in terms of burst morphology, width and bandwidth. This contradicts what has been shown for the repeater and non-repeater populations as a whole[4]. A careful comparison of, for example, the polarimetric properties of high-energy bursts from FRB 20201124A with those of non-repeaters may shed further light on their possible connections. If non-repeaters are indeed drawn from the high-energy tail of a repeater's burst energy distribution, then approximately 1,000 h of observing time, or more, is required to detect a repeat burst from a given source. Very few FRB sources have been observed in this way. On the other hand, if the observed flattening is a peculiarity of FRB 20201124A—and if the overall population of FRBs generally follows the steeper rate distribution as observed by FAST (and assuming all FRBs repeat)—then we can extrapolate this rate to the spectral energy density of our brightest burst, B06-st. Assuming a similar energy distribution as that observed by FAST, the rate of this burst is approximately 10^{-6} h^{-1}.

FRB 20201124A contributes strongly to the overall sky rate

The ASKAP FRB survey[29] was conducted in a similar frequency band as our observations. Based on modelled number counts[30] for 20 ASKAP bursts, $N(>F) = 20(F/50\,\mathrm{Jy\,ms})^{-1.5}$, and the total exposure (5.1×10^5 deg^2 h) of the ASKAP survey, an FRB all-sky rate above a fluence $F > 100$ Jy ms, $R_{\rm sky}(F > 100\,\mathrm{Jy\,ms}) = 5 \times 10^3$ sky^{-1} year^{-1} was reported[29]. During our campaign, we found 17 bursts from FRB 20201124A above this threshold, which, considering the amount of time spent on source, corresponds to 1.3% of $R_{\rm sky}(F > 100\,\mathrm{Jy\,ms})$. Moreover, considering only the three brightest bursts in our sample (those with $F > 500$ Jy ms), the contribution of FRB 20201124A to $R_{\rm sky}(F > 500\,\mathrm{Jy\,ms})$ during its active state is even twice as high, at 2.6%. Since the spectral energy distribution that we observe is shallower than the assumed power-law slope of −1.5 used in the modelled number counts[30], these fractional contributions are only a lower limit. This demonstrates that hyperactive repeaters may account for a substantial fraction of all observed FRBs.

FRB 20201124A would be observable even at very high redshift

The emission from FRB sources is subject to dispersion, scattering and Faraday rotation as it travels through the cold plasma of interstellar and intergalactic space. As such, the signals carry the imprints of

https://doi.org/10.1038/s41550-023-02153-z

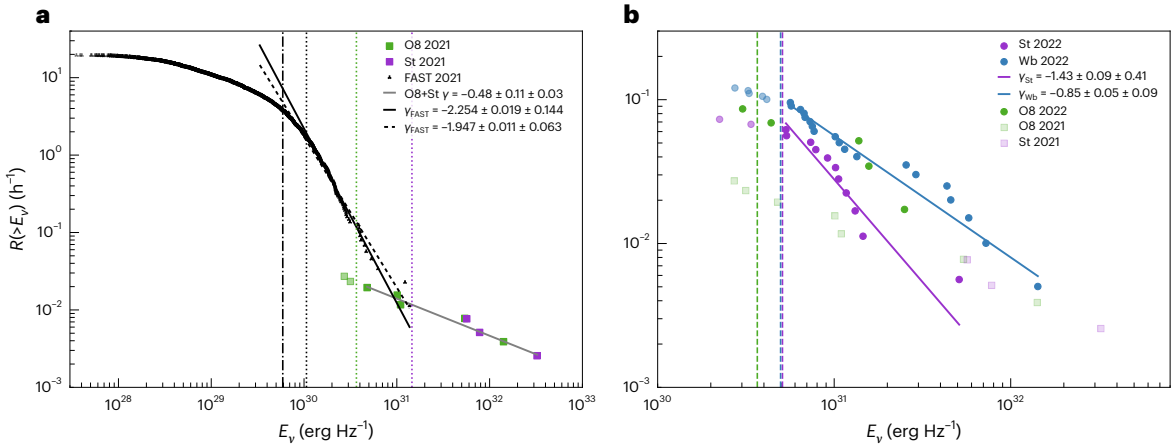

Fig. 3 | Burst spectral energy density distribution in different epochs. **a**, Cumulative burst rate distribution measured during the time range MJD 59,305–59,363 in comparison to those reported by FAST during the same epoch[20]. The vertical green and purple dotted lines indicate the completeness threshold for O8 and St, respectively, beyond which we jointly fitted the data with a simple power law (grey solid line). Pale coloured data points were excluded from the fit. The vertical black dotted and dash-dotted lines indicate the threshold beyond which the FAST data no longer follow a simple power law, as determined with the Python package powerlaw, and the break point of the broken power law as determined by Xu et al.[20], respectively. We fitted simple power laws to the data beyond the respective limits, as shown by the solid and dotted black lines. **b**, Coloured circles indicate the burst rates observed after MJD 59,602, as measured by Wb (blue), St (purple) and O8 (green). The coloured lines are the respective power-law fits. We did not fit the O8 data as there were too few detections. Note that in this time range, the St SEFD improved by a factor of ~3 compared to the data taken in 2021, lowering the completeness threshold compared to what is shown in **a**. For comparison, we also show the burst rates measured by O8 and St during the first activity window (pale coloured squares, same as **a**). The quoted uncertainties are composed of the statistical 1σ error of the least-squares fit (first error) and the 1σ uncertainty on the fitted slope from bootstrapping.

the matter density structure along a particular line of sight, allowing measurements of, for example, galaxy halo matter densities[31]. As the DM provides a complete measurement of the free electrons along the path, FRBs have already been used to trace the diffuse intergalactic medium and, thereby, have contributed to solving[32] the 'missing baryon problem'. Furthermore, it has been suggested[33] that individual, well-localized, gravitationally lensed, repeating FRBs could be used to measure the Hubble constant due to the change in the delays between the arrival times of lensed versions of subsequent bursts. As such, FRBs are proven cosmological probes with great future potential. How far back in cosmic history we can probe the Universe with FRBs is directly related to their energetics.

Assuming a burst bandwidth of 1 GHz, recent empirical models of the FRB population[14] find a characteristic spectral energy cutoff of $E_\nu^{\rm char} = 2.38^{+5.35}_{-1.64} \times 10^{32}\,{\rm erg\,Hz^{-1}}$. The most energetic burst that we report here, B06-st, had an isotropic-equivalent spectral energy of $E_\nu = 3.1^{+0.6}_{-0.7} \times 10^{32}\,{\rm erg\,Hz^{-1}}$, consistent with the estimated $E_\nu^{\rm char}$. For the FAST data shown in Fig. 3, the completeness threshold[20] was 53 mJy ms. Thus, given the spectral energy that we measured for B06-st, such a burst would have been observable out to redshift $z = 12.9^{+1.4}_{-1.5}$ with a telescope such as FAST.

At that redshift, the emitted frequency of the pulse would need to be ~19 GHz to be observable at 1.4 GHz from Earth. This is plausible, considering that FRB 20121102A has been detected at 8 GHz (ref. 34), which corresponds to an emission frequency of ~10 GHz at the source given its redshift[35] $z = 0.19273$. Similarly, to be observable in the CHIME band (400–800 MHz), pulses emitted at redshift $z = 12.9$ would need to be emitted at ~8 GHz at the source. Employing the Macquart relation[32], such a high redshift would imply DM ≈ 5,700 pc cm^{-3}. This is close to double the DM seen from any other FRB[1] to date. The largest measured FRB redshift[6] is currently $z = 1.016 \pm 0.002$. Nevertheless, purely from an energetics point of view, it is not implausible to expect hyperactive FRBs like FRB 20201124A at redshifts beyond 3, allowing for novel cosmological studies using repeat bursts. However, it has been pointed out[36] that at such high redshifts, individual bursts might be subject to scatter broadening as large as 300 ms at 1 GHz due to intervening galaxies. This would reduce the detectability of high-redshift FRBs.

Conclusions

Using four small 25–32 m class radio telescopes, we present a multi-frequency observing campaign targeting the hyperactive, repeating FRB 20201124A. This campaign is unprecedented in terms of the amount of observing time spent on source, and we conclude that ultra-high-energy bursts ($E_\nu \gtrsim 10^{31}\,{\rm erg\,Hz^{-1}}$) occur much more frequently than would have been expected based on previous observations of lower-energy bursts[20]. We argue that our detected bursts are intrinsically higher in energy, as opposed to being boosted in brightness by propagation effects like lensing.

Given our results, FRB 20201124A generates bursts spanning at least 6 orders of magnitude in spectral energy density, a similar span to the Galactic magnetar SGR 1935+2154 (ref. 37) but reaching much higher energies. Moreover, the burst energy distribution flattens towards the highest-observed energies. This high-energy distribution resembles that seen from the population of non-repeating FRBs as a whole, suggesting that observations of apparently non-repeating FRBs may simply be sampling the rare high-energy events of sources that are capable of repeating. The highest-energy bursts may originate from a separate emission mechanism or emission region at the progenitor source. Further evidence for such a scenario might be found by comparing the polarimetric properties of low- and high-energy bursts.

We also showed that FRB 20201124A's extremely energetic bursts, although rare, mean that a similar hyperactive repeating source would be detectable out to very high redshift ($z = 12$) using the world's most sensitive radio telescopes, although considerable on-sky time would be necessary to detect repeat bursts.

Lastly, the large number of high-fluence bursts ($F > 500$ Jy ms) that we detected from FRB 20201124A constitute an important fraction (at least ~2.6%) of the estimated all-sky FRB rate[29,30]. This shows that, in this high-fluence range, the all-sky rate is significantly influenced by a small number of hyperactive sources.

https://doi.org/10.1038/s41550-023-02153-z

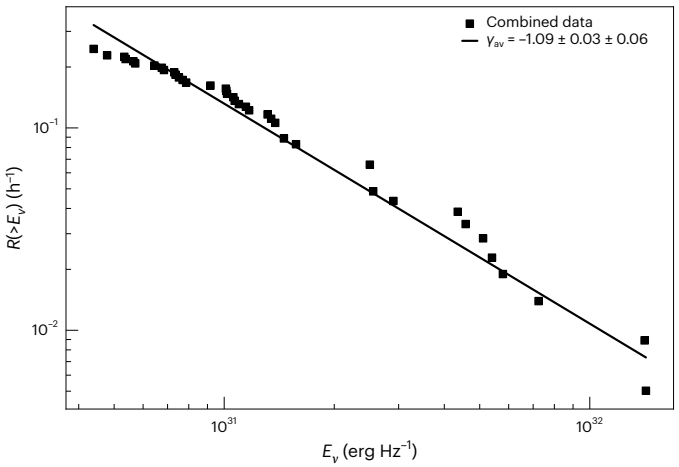

Fig. 4 | Burst energy distribution averaged over both activity windows. We excluded the data from St from the first activity window because of the large discrepancy in the detection threshold compared to the other stations. The solid black line denotes the best-fitting power law.

Methods

Observations and data reduction

Onsala, Westerbork and Toruń. O8, Wb and Tr recorded raw voltages (referred to as baseband data, providing both the amplitude and phase of the electromagnetic signal) in VDIF format[38] using the local DBBC2 and Flexbuff systems. Both left and right circular polarizations were sampled at the Nyquist rate and recorded as 2-bit samples. Depending on observing frequency and set-up, the recorded bandwidth varied between 64 and 512 MHz and was divided into sub-bands of 8, 16 or 32 MHz (Table 1). All observations made by O8 were conducted at L-band (between 1,202 and 1,714 MHz for various bandwidths). Wb covered P-band (300–364 MHz) when co-observing with the O8 and L-band when observing on its own. Tr observed at C-band (4,500–4,800 MHz for various bandwidths) when co-observing with another dish, or otherwise, it also covered a part of L-band. For the exact frequency ranges and observed hours per station, see Table 1.

All the data from Wb and O8 and a subset of the data from Tr were transferred using the internet to a dedicated processing machine, ebur, at the Onsala Space Observatory in Sweden. The processing pipeline[37] performed the following steps:

- Generate total-intensity (Stokes I) filterbanks (8-bit encoding) with various time and frequency resolutions from the baseband data.
- Search the filterbank data for bursts using Heimdall.
- Classify the candidates found by Heimdall using the machine learning classifier FETCH[39].
- Manually inspect the diagnostic plots generated by FETCH.

The time and frequency resolutions of the total-intensity filterbanks varied depending on the observing frequency: 1.024 ms and 7.8125 kHz at P-band, 0.128 ms and 62.5 kHz at L-band, and 0.064 ms and 500.0 kHz at C-band. These values were chosen as a compromise between the Nyquist limit and the maximal residual DM smearing in the lowest frequency channel of each observing band. In the Heimdall search, the DM range over which the search was conducted was limited to $DM_{FRB} \pm 50$ pc cm^{-3}, where $DM_{FRB} = 413.0$ pc cm^{-3}[15]. To mitigate the radio-frequency interference (RFI), we implemented a static frequency mask that was obtained through a manual inspection of parts of the data. The detection threshold was set to 7σ, which translates to fluence limits of roughly 42, 7 and 3 Jy ms at P-, L- and C- bands, respectively. When classifying the Heimdall-generated burst candidates as either astronomical signals or RFI, we used FETCH models[39] a and h with a probability threshold of 0.5.

Stockert. The recording set-up and burst detection pipeline at St were developed independently from the one for O8, Wb and Tr, and hence, it uses different tools and detection thresholds. At St, we observed in the frequency range 1,332.5–1,430.5 MHz, recording total-intensity 32-bit data with a pulsar fast Fourier transform back end[40]. The data were initially stored as PFFTS files, which is the instrument's specific format. These were subsequently converted to the standardized filterbank format using the tool filterbank, which is part of the SIGPROC package[41]. The resulting data had time and frequency resolutions of 218.45 µs and 586 kHz and were stored as 32-bit floats. We used the tools rfifind, prepsubband and single_pulse_search from the PRESTO package[42] to subsequently remove RFI, incoherently dedisperse the data (using DM = 412.0 pc cm^{-3}) and search for bursts. Between 24 November 2021 and 8 February 2022, the St dish underwent an upgrade, reducing the system equivalent flux density (SEFD) by almost a factor of 3 (Table 1), thereby improving the sensitivity of the dish substantially. We used a detection threshold of 8σ in the pulse searches, which corresponds to fluence limits of 21 and 7 Jy ms before and after the upgrade, respectively.

Digitization artefacts. As discussed above, we recorded 2-bit baseband data at O8, Wb and Tr. The limited dynamic range of these samples in combination with the large fluences of some of the bursts (signal-to-noise (S/N) ratio ≈ 100) leads to digitization artefacts in the data whereby power is 'scattered' in time and frequency[43]. Most notably this manifests as 'depressions' in the data around the times of the bursts (for example, burst B08-o8 in Extended Data Fig. 4). A similar digitization artefact was also found and described[44] for a burst from FRB 20201124A detected at 2.2 GHz. As a result, the measured overall fluences will be underestimated. To quantify this effect and compensate for it, we measured the fluences from data products generated from the baseband data in three different ways. For case i, we created coherently dedispersed total-intensity filterbanks with SFXC, the Super FX Correlator[45]. These filterbank data were subsequently converted to archive files with DSPSR, the standard pulsar software package[46]. For case ii, we used the tool digifil that is part of DSPSR to generate total-intensity filterbanks (no dedispersion applied), which we then converted to archives with DSPSR (applying incoherent dedispersion). For case iii, we applied a scattered power correction (SPC) algorithm[47] that is part of PSRCHIVE[48,49] to the archives generated in case ii.

The reason for implementing case iii is that digifil applies a 2-bit correction to the baseband data[43] that effectively overcompensates for the limited dynamic range of bright bursts. The effect is that the overall measured fluence is overestimated compared to the real fluence. Extended Data Fig. 4 compares the burst profiles for B08-o8 generated in these three ways. The profile generated from SFXC dips below the mean of the off-pulse region between components. In contrast, the profile generated by the regular digifil stays above the mean. Even though this could be intrinsic to the pulse, that the profile appears to begin/rise early compared to the SFXC profile indicates that there is an overall 'skirt' around the burst that is due to the 2-bit correction implemented in digifil. The profile generated from the archive corrected with the SPC algorithm (case iii) does not show this skirt and also does not drop below the mean between components. Thus, we conclude that this data product provides the best estimate of the true fluence of the burst. Extended Data Fig. 5 shows a relative comparison of the measured fluences scaled by the SPC-corrected fluences. Overall, compared to the case iii fluences, the case ii fluences (uncorrected digifil) are 5–10% higher, whereas the case i fluences (SFXC generated) are lower by a factor 1.5–2.0. There is no clear fluence threshold above which the quantization limitation shows its effects. Rather, it is the range in the time–frequency space over which power is concentrated that determines whether or not 'depressions' occur. A single bright scintil can result in scattered power whereas the overall band-integrated fluence is not higher compared to other bursts. Although making these

corrections is important for achieving the most accurate fluences possible, note that the factor of 2 uncertainties in the burst energies do not affect the conclusions that we draw in this paper.

For the data recorded at St, the 2-bit quantization limitations did not apply, and we measured the burst properties directly from the recorded filterbanks and the archive files generated for case ii.

Analysis and results

DM optimization. We used the structure-optimizing code DM-phase[23] on one of our brightest multi-component bursts (B13-o8, Fig. 2) to obtain DM = 410.8 ± 0.3 pc cm^{-3} (DM-phase uses a DM constant of 1/0.000241 GHz^2 cm^3 pc^{-1} μs). To assess any potential evolution of the DM over the roughly 1-year time span of our observing campaign, we ran DM-phase on nine other bright, multi-component bursts detected throughout the campaign. We did not measure any significant evolution nor any DM values that disagree beyond their respective 2σ uncertainties with our initial measurement (Extended Data Table 2). Any DM offsets on the order of our measurement uncertainties have only a negligible impact on the values listed in Extended Data Table 3 (the most notable would be a difference in the TOA of ~1.2 ms for a DM offset of 0.5 pc cm^{-3}). Thus, given the challenges in measuring the 'correct' DM of an FRB[50], we used this DM value in the rest of the analysis for all detected bursts.

The effect of bandwidth on the number of detected bursts. During our campaign, we detected bursts spanning more than an order of magnitude in spectral energy E_ν. A power-law slope like the one observed with FAST[20] would require a difference in rate of a factor of $\gtrsim 10^2$ between the high- and low-energy bursts, that is a factor ≥10 larger than what we find. Previous studies[11] of FRB 20121102A reported that low-energy bursts ($E_\nu \lesssim 3 \times 10^{29}$ erg Hz^{-1}) were typically narrower in bandwidth than high-energy bursts. In our case, this could imply that due to our limited bandwidth of ~100 MHz, we might miss low-energy bursts as they might be bright outside of our observing band. In contrast, the high-energy bursts are sufficiently broadband to always fall within our frequency window. Conversely, the FAST L-band receiver covers a frequency range of 1.0–1.5 GHz, and the median bandwidth[20] of the bursts (185 MHz) indicates that bursts with different central frequencies appear in different parts of the FAST L-band so that these may be outside our limited frequency range. However, the cumulative burst rate that we derive for our 'low-energy' bursts ($E_\nu \approx 10^{31}$ erg Hz^{-1}) is in good agreement with similarly energetic bursts detected with FAST[20] in the same time range. Therefore, we exclude the possibility that we missed a large fraction of bursts because of a frequency 'windowing' effect. Even if we had missed some of the low-energy bursts because of RFI, we deem it highly unlikely that we had missed 90% of the possible low-energy bursts. Instead, we conclude that we detected a factor of ~10 'too many' bursts compared to what one would expect from the FAST slope[20] in the spectral energy range ~10^{30}–10^{32} erg Hz^{-1} during this period.

Burst properties. Except for the TOA, all burst properties listed in Extended Data Table 3 were obtained from the archive files that were corrected with the SPC algorithm (case iii above). First, we manually determined a flagging mask using the PSRCHIVE tools pazi and psrzap. This mask excises RFI and discards 5% of bandwidth at the top and bottom of each sub-band. We subsequently downsampled the data to time and frequency resolutions of 256 μs and 500 kHz, respectively, inspected the dedispersed burst profiles by eye and manually selected the start and stop bins of burst components. For each of these (component-based) time ranges, we computed the two-dimensional autocorrelation function in time and frequency. The resulting autocorrelation spectra and time series were fitted separately with a one-dimensional Gaussian to determine the component width in time (the time Gaussian) and in frequency (the frequency Gaussian). To measure the scintillation bandwidth for each burst component, we first subtracted the frequency Gaussian from the autocorrelation spectra and then fitted a Lorentzian to the central component of the residuals. The half-width at half-maximum of this Lorentzian is an estimate of the scintillation bandwidth ν_s (ref. 51). We list these values scaled to a frequency of 1 GHz in Extended Data Table 3. For the scaling of ν_s with central frequency ν_c, $\nu_s \propto \nu_c^\alpha$, we adopted a canonical power-law slope $\alpha = 4.0$. The median of $\nu_s^{1\,\mathrm{GHz}} = 0.4 \pm 0.1$ MHz is consistent with earlier measurements[24]. Finally, we took the burst frequency extent to be the total observing bandwidth, unless twice the full-width at half-maximum (FWHM) of the frequency Gaussian was less than 75% of the total bandwidth (BW, that is 2 × FWHM < 0.75 × BW), in which case we determined by eye the burst frequency extent. This approach was chosen to ensure that no flux was lost due to flagged channels (which in either case would lead to an underestimated FWHM of the frequency Gaussian). The fluences were computed by first determining the flux densities per time bin using the radiometer equation[52]. We assumed a constant gain and constant system temperature, yielding the SEFDs listed in Table 1. Subsequently, we summed over the manually selected on-time region. From the fluences, we then determined the isotropic-equivalent spectral luminosity of the bursts using the known luminosity distance[53] $D_L = 453 \pm 0.1$ Mpc ($z = 0.098$) of FRB 20201124A.

Burst times of arrival. It is not uncommon for some data loss to occur during recording (of the order of a few seconds accumulated over a 15 min recording). digifil has currently no functionality to detect and account for such data loss, which eventually leads to inaccurate timestamps in the generated filterbanks. Having been developed for correlating interferometric observations, SFXC has the required functionality to compensate for such losses. Therefore. we used SFXC to generate coherently dedispersed filterbanks (SFXC uses the same DM constant as DM-phase) to compute the TOA of each burst component. We fitted multi-component Gaussians to the frequency-averaged profile (time resolution of 64 μs) of each burst and took the centre of each Gaussian component as the component's TOA. The timestamps in the SFXC-generated filterbanks were referenced to the geocentre. The reference frequency used for coherently dedispersing the pulses was the centre frequency of the highest sub-band. In Extended Data Table 3, the listed TOAs are referenced to the barycentre (using the barycentric dynamical time) at infinite frequency. The times designate either the middle between the first and the last component of a multi-component burst or the centre of the fitted Gaussian for single-component bursts. Extended Data Fig. 6 displays the log-normal distribution of time separation between components of multi-component bursts. The Gaussian fit yields a characteristic separation of $\delta t = 4.1^{+4.4}_{-2.1}$ ms between burst components, which is a factor 2–10 larger than that reported[22] for FRB 20121102A.

Burst rates. The distribution of bursts that we detected shows no evidence of a broken power law, which is why we fitted a simple power law for the cumulative burst rate as a function of spectral energy density, $R(>E_\nu) \propto E_\nu^\gamma$, using a least-squares method. For the fitting, we set conservative 15σ completeness limits (assuming a canonical burst width of 1 ms) of 10 and 39 Jy ms for O8 and St, respectively, and we adopted a 20% uncertainty on the derived spectral energy density. To better estimate the uncertainties of the fitted parameters, we fitted the entire dataset and we also ran a bootstrapping algorithm for which we randomly selected 90% of the data points (without replacement) and performed the least-squares fit on this subset of data. We repeated the bootstrapping step 1,000 times and took the standard deviation of the fitted parameters as the additional bootstrapping error. Jointly fitting the O8 and St data yielded a power-law index $\gamma = -0.48 \pm 0.11 \pm 0.03$. We also fitted the contemporaneous FAST data[20] in a similar fashion. We first applied our definition of a unique burst to the FAST data by summing fluences of bursts that are separated by less

than 100 ms. This affected a total of 148 bursts detected by FAST. We then determined the threshold $E_\nu^{\rm min}$ below which the high-energy part of the FAST bursts no longer followed a simple power law using the Python powerlaw[54] package and fitted the data for which $E > E_\nu^{\rm min} = 1.7 \times 10^{30}$ erg Hz^{-1}, in the same way as described above. We found $\gamma_{\rm FAST} = -2.254 \pm 0.019 \pm 0.114$, which is even steeper than the reported[20] $\gamma_2 = -1.5 \pm 0.1 \pm 0.1$. Xu et al.[20] found the break point between the low- and high-energy ranges of their burst distribution to be ~1.1×10^{38} erg (= 5.9×10^{29} erg Hz^{-1} using their median bandwidth of 185 MHz to convert from energy to spectral energy density), roughly a factor 3 lower than our adopted $E_\nu^{\rm min}$. Using the break point from Xu et al.[20] as the limiting energy for the fit, we found $\gamma_{\rm FAST} = -1.947 \pm 0.011 \pm 0.063$, which agrees with γ_2 within 2σ.

For completeness, we also fitted the FAST data without summing components that are separated by less than 100 ms. This yielded values for $\gamma_{\rm FAST}$ of $-2.318 \pm 0.018 \pm 0.116$ (when determining the power-law break point with the software powerlaw) and $-1.997 \pm 0.011 \pm 0.067$ (using the published break point[20]), which agree within the uncertainties for the values found when applying our definition of a unique burst.

The bursts and the associated cumulative burst rates that we detected with O8, Wb and St after MJD 59,602 are shown in Fig. 3b. We fitted the data from Wb and St in the same way as described above, using, however, a 15σ completeness limit of 14 Jy ms for both telescopes (because of the upgrade at St discussed above). We did not fit the bursts detected at O8 separately because of the low number of detections. The burst rates we found are $\gamma_{\rm Wb} = -1.43 \pm 0.09 \pm 0.41$ and $\gamma_{\rm St} = -0.85 \pm 0.05 \pm 0.09$ for the Wb and St bursts, respectively.

Implications of non-detections at P- and C-band. As listed in Table 1, we spent about 650 h observing FRB 20201124A at P-band with Westerbork, and another 244 h observing at C-band with Toruń. If we consider the time windows with enhanced activity only, that is MJD 59,305–59,363 and MJD 59,602–59,641 (Fig. 1), these numbers reduce to 274 and 36 h for P-band and to 115 h and 86 h for the C-band observations, respectively. During the same two time ranges, we spent a total of 513 and 351 h of non-overlapping time on source at L-band. The completeness thresholds for the P- and C-bands are ~91 and ~5 Jy ms, respectively. Extended Data Table 1 lists the number of bursts that we detected at L-band above a given fluence threshold; once assuming a flat spectrum for the bursts and once assuming a steep spectrum with $\alpha = -1.5$. Given the number of bursts detected at L-band and the time that each band was observed for, we also list the number of bursts that we would have expected to detect at P- and C-bands if we assume that the activity rates are the same across all observed frequencies. The expected number of bursts ranges between 0.6 and 7.6, depending on the observing band and epoch considered. That we did not detect a single burst outside L-band clearly shows that the bursts are narrowband in nature[55,56] and that the activity rates and, potentially, even the activity windows are frequency dependent[57,58]. Alternatively, besides the spectral index, the emission process might be such that the amplitude of the bursts is modulated as a function of frequency, peaking in the range 1,200–1,700 MHz during our observations. Whatever the modulation mechanism might be (intrinsic to the source or a propagation effect such as refractive scintillation), it has to be time variable as the source was first detected by CHIME/FRB in the band between 400 and 800 MHz (ref. 15).

The notch in burst B08. We note a curious feature in burst B08, which is highlighted in Supplementary Fig. 1 for B08-tr (this can also be seen in Extended Data Fig. 4, which shows the same burst detected by O8, B08-o8). We call this sudden, sharp dip in flux density a 'notch'. The B08 notch, lasting ~0.5 ms, is somewhat reminiscent of the notches seen in the average profiles of a few very bright radio pulsars[59], which also happen to have exceptionally wide pulse profiles that cover a large range of rotational phases. However, pulsar notches are double notches (two closely spaced dips), whereas the limited S/N ratio of B08 makes it impossible to see more subtle features in the notch profile. This limits the degree to which we can compare the two phenomena.

For pulsars, the notches have been modelled as coming from an absorbing region in an outer magnetosphere that co-rotates with the neutron star[60]. This model requires that the pulsar has both emitting and absorbing regions at heights that are a large fraction of the light cylinder radius. In another model[61], the pulsar itself is the absorber and the emission is a combination of inward- and outward-travelling components.

FRBs often show quite well-defined sub-bursts with cessation of emission between these components[22]. This is also clearly visible in B08 (Supplementary Fig. 1, left panel). However, the notch we detect in B08 appears qualitatively different. It is a sudden, sharp dip on the shoulder of a bright component, much like what is seen in pulsar notches (Supplementary Fig. 1, right panel). We speculate that notches may be generally visible in the profiles of high S/N ratio, wide FRBs observed at high time resolution, and that this effect could plausibly probe magnetospheric physics, assuming such an origin for FRB emission. Furthermore, if notches can be detected in several bursts from a single repeater, then these could provide a stable marker of rotational phase that could allow the spin rate of the neutron star to be determined. This assumes that the absorber is locked in rotational phase with respect to the neutron star. For pulsars, the notches indeed occur at stable rotational phases, which can be explained by the models[60,61] mentioned above. FRB notches would also potentially be excellent reference points for determining accurate DMs. As can be seen in Supplementary Fig. 1, the notch occurs at the same time across the observed radio-frequency band for the DM we have chosen to dedisperse all bursts in the paper.

Data availability

The data that support the plots within this paper and other findings of this study are available under https://doi.org/10.5281/zenodo.10006349 or from the corresponding author upon reasonable request.

Code availability

The pipeline written to process the baseband data can be found at https://github.com/pharaofranz/frb-baseband. The scripts used to analyse the data and generate the plots for this paper are available at https://github.com/astroflash-frb/frb20201124A-kirsten-2023. jive5ab can be retrieved from https://github.com/jive-vlbi/jive5ab, Heimdall is hosted at https://sourceforge.net/projects/heimdall-astro/ and FETCH can be found at https://github.com/devanshkv/fetch. The pulsar package DSPSR is hosted at https://sourceforge.net/projects/dspsr/. SIGPROC was retrieved from https://github.com/SixByNine/sigproc.

References

1. CHIME/FRB Collaboration. The First CHIME/FRB Fast Radio Burst Catalog. *Astrophys. J. Suppl. Ser.* **257**, 59 (2021).
2. Spitler, L. G. et al. A repeating fast radio burst. *Nature* **531**, 202–205 (2016).
3. Andersen, B. C. et al. CHIME/FRB discovery of 25 repeating fast radio burst sources. *Astrophys. J.* **947**, 83 (2023).
4. Pleunis, Z. et al. Fast radio burst morphology in the first CHIME/FRB catalog. *Astrophys. J.* **923**, 1 (2021).
5. CHIME/FRB Collaboration. A bright millisecond-duration radio burst from a Galactic magnetar. *Nature* **587**, 54–58 (2020).
6. Ryder, S. D. et al. A luminous fast radio burst that probes the Universe at redshift 1. *Science* **382**, 294–299 (2023).
7. Li, D. et al. A bimodal burst energy distribution of a repeating fast radio burst source. *Nature* **598**, 267–271 (2021).
8. Zhang, Y.-K. et al. FAST observations of an extremely active episode of FRB 20201124A. II. Energy distribution. *Res. Astron. Astrophys.* **22**, 124002 (2022).

9. Kumar, P. et al. Spectropolarimetric variability in the repeating fast radio burst source FRB 20180301A. *Mon. Not. R. Astron. Soc.* **526**, 3652–3672 (2023).
10. Jahns, J. N. et al. The FRB 20121102A November rain in 2018 observed with the Arecibo Telescope. *Mon. Not. R. Astron. Soc.* **519**, 666–687 (2023).
11. Hewitt, D. M. et al. Arecibo observations of a burst storm from FRB 20121102A in 2016. *Mon. Not. R. Astron. Soc.* **515**, 3577–3596 (2022).
12. James, C. W. et al. The fast radio burst population evolves, consistent with the star formation rate. *Mon. Not. R. Astron. Soc.* **510**, L18–L23 (2022).
13. Lu, W., Beniamini, P. & Kumar, P. Implications of a rapidly varying FRB in a globular cluster of M81. *Mon. Not. R. Astron. Soc.* **510**, 1867–1879 (2022).
14. Shin, K. et al. Inferring the energy and distance distributions of fast radio bursts using the first CHIME/FRB catalog. *Astrophys. J.* **944**, 105 (2023).
15. CHIME/FRB Collaboration. Recent high activity from a repeating fast radio burst discovered by CHIME/FRB. *Astron. Telegr.* **14497**, 1 (2021).
16. Wang, P. et al. FAST detect sustained activities and a bright burst from FRB20201124A. *Astron. Telegr.* **15288**, 1 (2022).
17. Ould-Boukattine, O. S. et al. Burst detection from FRB 20201124A using the Westerbork-RT1 25-m telescope. *Astron. Telegr.* **15190**, 1 (2022).
18. Piro, L. et al. The fast radio burst FRB 20201124A in a star-forming region: constraints to the progenitor and multiwavelength counterparts. *Astron. Astrophys.* **656**, L15 (2021).
19. Fong, W.-F. et al. Chronicling the host galaxy properties of the remarkable repeating FRB 20201124A. *Astrophys. J. Lett.* **919**, L23 (2021).
20. Xu, H. et al. A fast radio burst source at a complex magnetized site in a barred galaxy. *Nature* **609**, 685–688 (2022).
21. Atri, P. et al. Detection of two bright bursts from FRB20201124A with Apertif at the Westerbork Synthesis Radio Telescope. *Astron. Telegr.* **15197**, 1 (2022).
22. Hessels, J. W. T. et al. FRB 121102 bursts show complex time–frequency structure. *Astrophys. J. Lett.* **876**, L23 (2019).
23. Seymour, A., Michilli, D. & Pleunis, Z. DM_phase: Algorithm for correcting dispersion of radio signals. *Astrophysics Source Code Library*, record ascl:1910.004 (2019).
24. Main, R. A. et al. Scintillation time-scale measurement of the highly active FRB20201124A. *Mon. Not. R. Astron. Soc.* **509**, 3172–3180 (2022).
25. Cordes, J. M. et al. Lensing of fast radio bursts by plasma structures in host galaxies. *Astrophys. J.* **842**, 35 (2017).
26. Narayan, R. & Wallington, S. Magnification bias and gravitational lensing statistics. In *Proc. Liege International Astrophysical Colloquia*, Vol. 31 (eds Surdej, J. et al.) 217 (Univ. of Liège, 1993).
27. Oguri, M. Strong gravitational lensing of explosive transients. *Rep. Prog. Phys.* **82**, 126901 (2019).
28. Main, R. et al. Pulsar emission amplified and resolved by plasma lensing in an eclipsing binary. *Nature* **557**, 522–525 (2018).
29. Shannon, R. M. et al. The dispersion-brightness relation for fast radio bursts from a wide-field survey. *Nature* **562**, 386–390 (2018).
30. Lu, W. & Piro, A. L. Implications from ASKAP fast radio burst statistics. *Astrophys. J.* **883**, 40 (2019).
31. Prochaska, J. X. et al. The low density and magnetization of a massive galaxy halo exposed by a fast radio burst. *Science* **366**, 231–234 (2019).
32. Macquart, J. P. et al. A census of baryons in the Universe from localized fast radio bursts. *Nature* **581**, 391–395 (2020).
33. Wucknitz, O., Spitler, L. G. & Pen, U. L. Cosmology with gravitationally lensed repeating fast radio bursts. *Astron. Astrophys.* **645**, A44 (2021).
34. Gajjar, V. et al. Highest frequency detection of FRB 121102 at 4–8 GHz using the breakthrough listen digital backend at the Green Bank Telescope. *Astrophys. J.* **863**, 2 (2018).
35. Tendulkar, S. P. et al. The host galaxy and redshift of the repeating fast radio burst FRB 121102. *Astrophys. J. Lett.* **834**, L7 (2017).
36. Ocker, S. K. et al. Radio scattering horizons for galactic and extragalactic transients. *Astrophys. J.* **934**, 71 (2022).
37. Kirsten, F. et al. Detection of two bright radio bursts from magnetar SGR 1935 + 2154. *Nat. Astron.* **5**, 414–422 (2021).
38. Whitney, A. et al. VLBI Data Interchange Format (VDIF). In *Proc. 6th International VLBI Service for Geodesy and Astronomy* (eds Navarro, R. et al.) 192–196 (NASA, 2010).
39. Agarwal, D. et al. FETCH: a deep-learning based classifier for fast transient classification. *Mon. Not. R. Astron. Soc.* **497**, 1661–1674 (2020).
40. Barr, E. D. et al. The Northern High Time Resolution Universe pulsar survey. I. Setup and initial discoveries. *Mon. Not. R. Astron. Soc.* **435**, 2234–2245 (2013).
41. Lorimer, D. R. SIGPROC: pulsar signal processing programs. *Astrophysics Source Code Library*, record ascl:1107.016 (2011).
42. Ransom, S. PRESTO: pulsar exploration and search toolkit. *Astrophysics Source Code Library*, record ascl:1107.017 (2011).
43. Jenet, F. A. & Anderson, S. B. The effects of digitization on nonstationary stochastic signals with applications to pulsar signal baseband recording. *Publ. Astron. Soc. Pac.* **110**, 1467–1478 (1998).
44. Ikebe, S. et al. Detection of a bright burst from the repeating fast radio burst 20201124A at 2 GHz. *Publ. Astron. Soc. Jpn* **75**, 199–207 (2023).
45. Keimpema, A. et al. The SFXC software correlator for very long baseline interferometry: algorithms and implementation. *Exp. Astron.* **39**, 259–279 (2015).
46. van Straten, W. & Bailes, M. DSPSR: digital signal processing software for pulsar astronomy. *Pubs. Astron. Soc. Aust.* **28**, 1–14 (2011).
47. van Straten, W. High-fidelity radio astronomical polarimetry using a millisecond pulsar as a polarized reference source. *Astrophys. J. Suppl. Ser.* **204**, 13 (2013).
48. van Straten, W., Demorest, P. & Oslowski, S. Pulsar data analysis with PSRCHIVE. *Astron. Res. Technol.* **9**, 237–256 (2012).
49. Hotan, A. W., van Straten, W. & Manchester, R. N. PSRCHIVE and PSRFITS: an open approach to radio pulsar data storage and analysis. *Publ. Astron. Soc. Aust.* **21**, 302–309 (2004).
50. Nimmo, K. et al. A burst storm from the repeating FRB 20200120E in an M81 globular cluster. *Mon. Not. R. Astron. Soc.* **520**, 2281–2305 (2023).
51. Rickett, B. J. Radio propagation through the turbulent interstellar plasma. *Annu. Rev. Astron. Astrophys.* **28**, 561–605 (1990).
52. Cordes, J. M. & McLaughlin, M. A. Searches for fast radio transients. *Astrophys. J.* **596**, 1142–1154 (2003).
53. Ravi, V. et al. The host galaxy and persistent radio counterpart of FRB 20201124A. *Mon. Not. R. Astron. Soc.* **513**, 982–990 (2022).
54. Alstott, J., Bullmore, E. & Plenz, D. powerlaw: a Python package for analysis of heavy-tailed distributions. *PLoS ONE* **9**, e85777 (2014).
55. Majid, W. A. et al. A dual-band radio observation of FRB 121102 with the Deep Space Network and the detection of multiple bursts. *Astrophys. J. Lett.* **897**, L4 (2020).
56. Gourdji, K. et al. A sample of low-energy bursts from FRB 121102. *Astrophys. J. Lett.* **877**, L19 (2019).
57. Pleunis, Z. et al. LOFAR detection of 110–188 MHz emission and frequency-dependent activity from FRB 20180916B. *Astrophys. J. Lett.* **911**, L3 (2021).
58. Pastor-Marazuela, I. et al. Chromatic periodic activity down to 120 megahertz in a fast radio burst. *Nature* **596**, 505–508 (2021).
59. McLaughlin, M. A. & Rankin, J. M. 'Notches' in the average profiles of bright pulsars. *Mon. Not. R. Astron. Soc.* **351**, 808–812 (2004).

60. Wright, G. A. E. A model for 'double notches' in radio pulsar profiles. *Mon. Not. R. Astron. Soc.* **351**, 813–822 (2004).
61. Dyks, J. et al. The pulsar shadow as the origin of double notches in radio pulse profiles. *Astrophys. J.* **633**, 1101–1113 (2005).

Acknowledgements

We thank the directors and staff at the various participating telescopes for allowing us to use their facilities and for helping to make the observations. We express our gratitude to W. van Straten for modifying the DSPSR software package to fit our needs and for helping with the SPC algorithm. F.K. acknowledges support from the Onsala Space Observatory for the provisioning of its facilities and observational support. The national research infrastructure at the Onsala Space Observatory is funded through Swedish Research Council grant no. 2017-00648. Research by the AstroFlash group at the University of Amsterdam, ASTRON and JIVE is supported in part by a Vici grant from the Dutch Scientific Research Council (*Nederlandse Oranisatie voor Wetenschappelijk Onderzoek* or NWO; PI Hessels; VI.C.192.045). ASTRON is the Netherlands Institute for Radio Astronomy and an institute of the NWO. This work was supported by an NWO XS grant: WesterFlash (OCENW.XS22.1.053; PI: Kirsten). K.N. is a Kavli fellow at the Massachusetts Institute of Technology. This work is based in part on observations carried out using the 32 m radio telescope operated by the Institute of Astronomy of the Nicolaus Copernicus University in Toruń (Poland) and supported by a Polish Ministry of Science and Higher Education SpUB grant. This work makes use of data from the Westerbork Synthesis Radio Telescope owned by ASTRON. We thank the Westerbork operators R. Blauw, J. J. Sluman and H. Mulders for scheduling observations.

Author contributions

F.K. wrote and ran the search pipeline, led the observations at Onsala, interpreted the data and led the paper writing. O.S.O.B led the observations at Westerbork, created Figs. 1–4 and Extended Data Figs. 1–3. W.H. led the observations at Stockert, searched the Stockert data for bursts and described the observations. M.P.G. led the observations at Toruń and searched the data for bursts. J.W.T.H. interpreted the data scientifically, supervised the student work and wrote parts of the paper. W.L. interpreted the data scientifically and commented on the paper. M.P.S., P.C., K.N. and R.v.R commented on the paper. J.Y. supported the observations at Onsala. R.B. supported the observations at Westerbork. W.P. and P.W. supported the observations at Toruń.

Funding

Open access funding provided by Chalmers University of Technology.

Competing interests

The authors declare no competing interests.

Additional information

Extended data Extended data are available for this paper at https://doi.org/10.1038/s41550-023-02153-z.

Supplementary information The online version contains supplementary material available at https://doi.org/10.1038/s41550-023-02153-z.

Correspondence and requests for materials should be addressed to F. Kirsten.

Peer review information *Nature Astronomy* thanks Deborah Good and Yongkun Zhang for their contribution to the peer review of this work.

https://doi.org/10.1038/s41550-023-02153-z

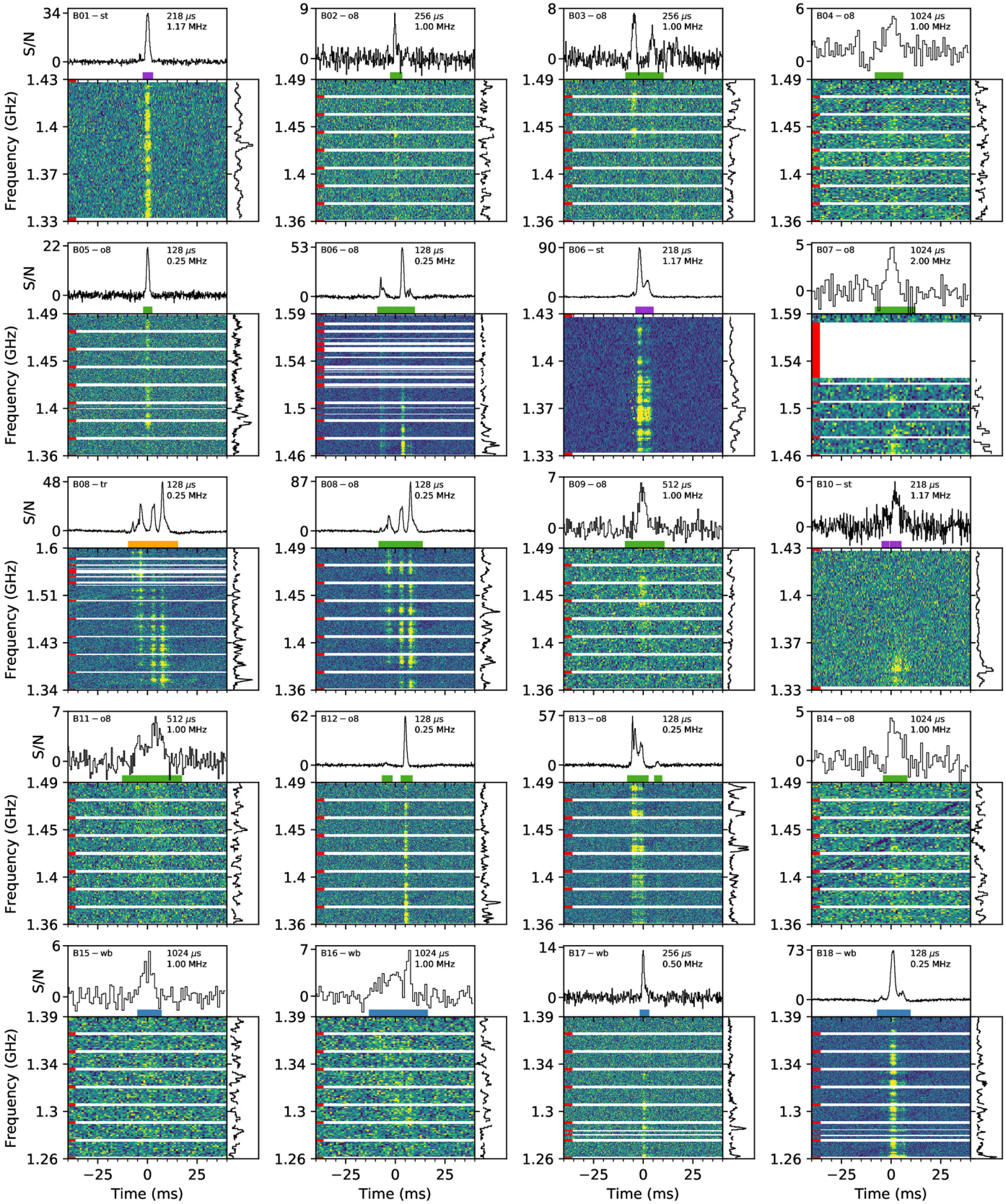

Extended Data Fig. 1 | Collection of all bursts detected in this campaign, part I. See Fig. 2 for a full description of the sub-panels.

https://doi.org/10.1038/s41550-023-02153-z

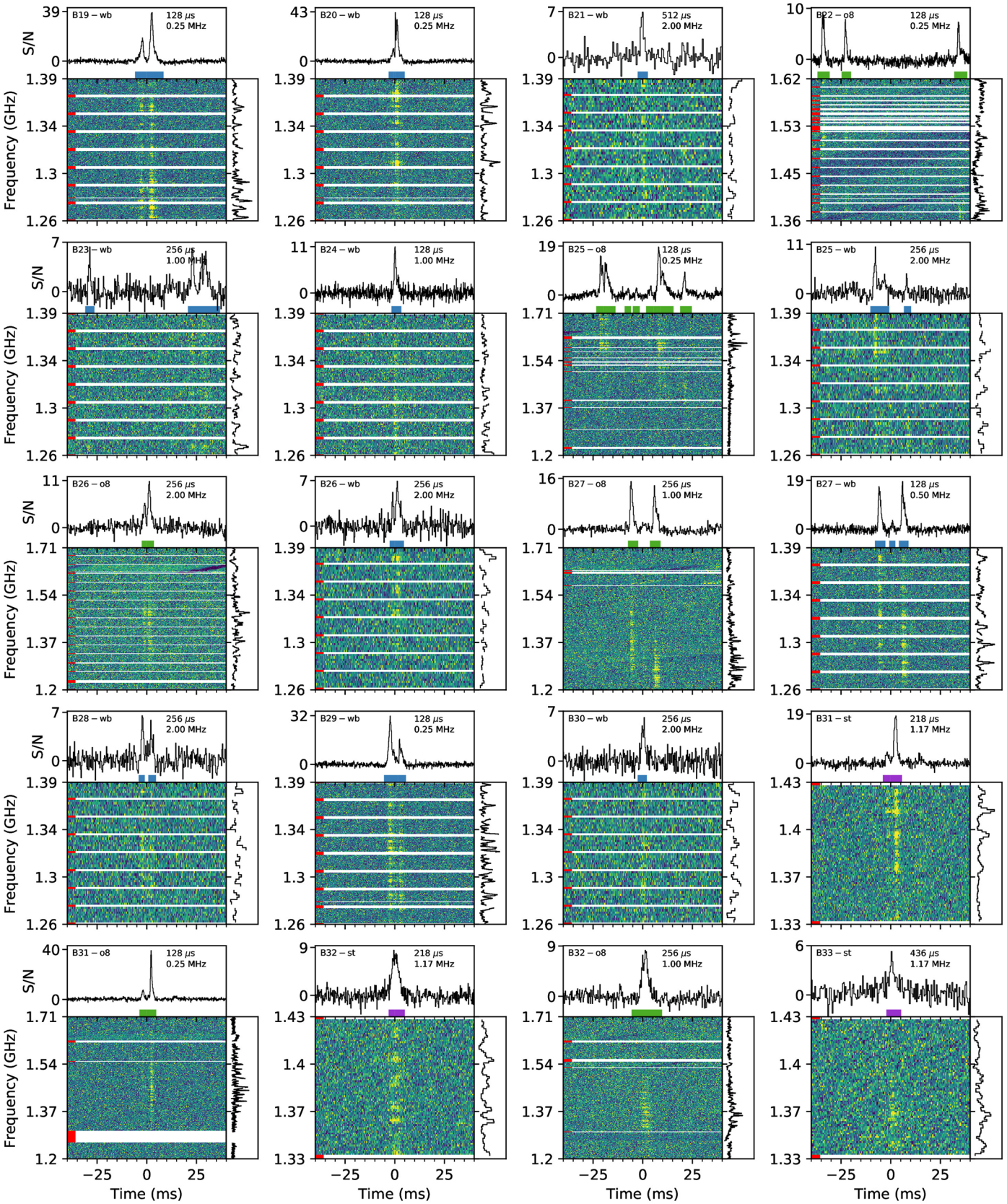

Extended Data Fig. 2 | Collection of all bursts detected in this campaign, part II. See Fig. 2 for a full description of the sub-panels.

https://doi.org/10.1038/s41550-023-02153-z

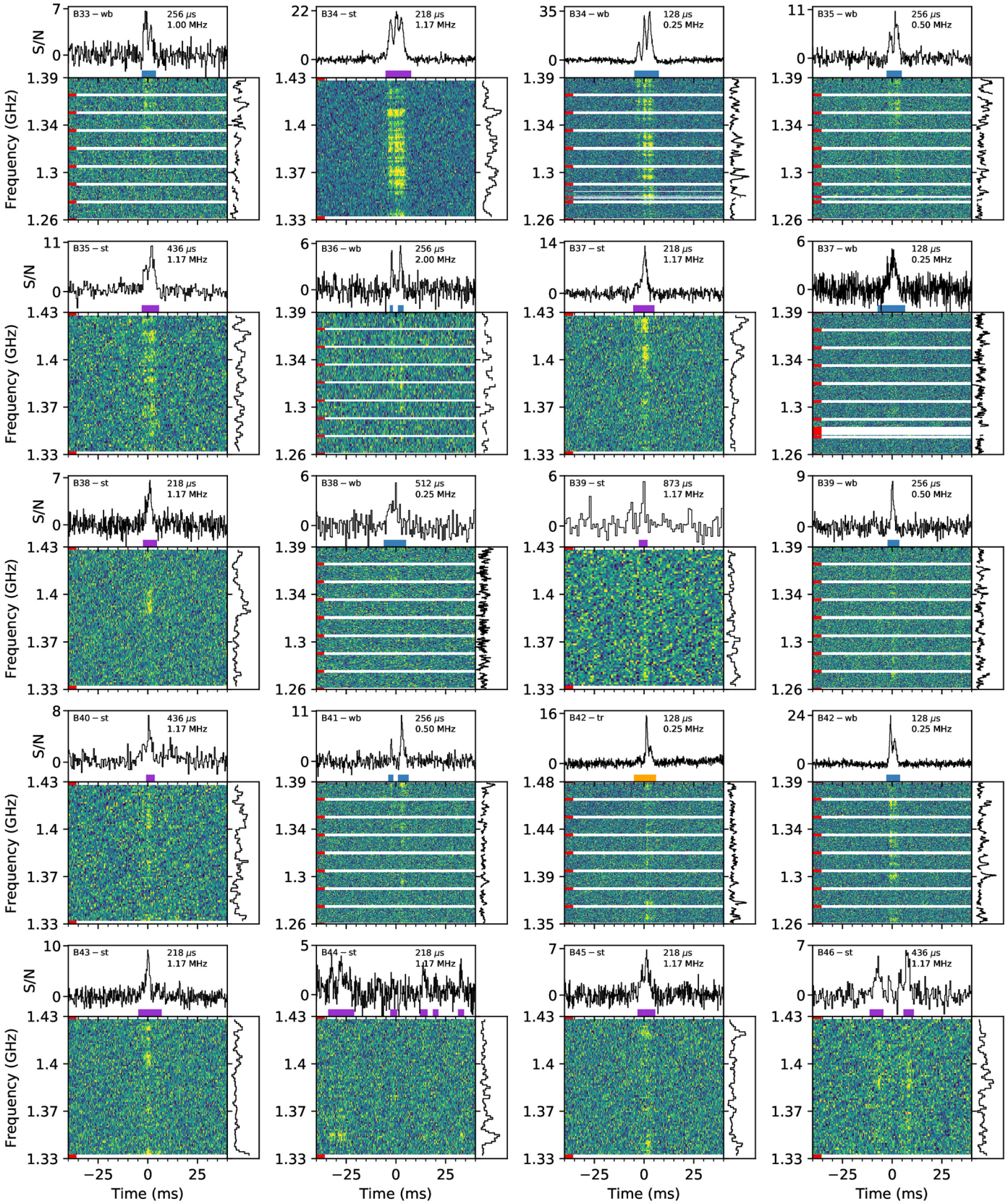

Extended Data Fig. 3 | Collection of all bursts detected in this campaign, part III. See Fig. 2 for a full description of the sub-panels.

https://doi.org/10.1038/s41550-023-02153-z

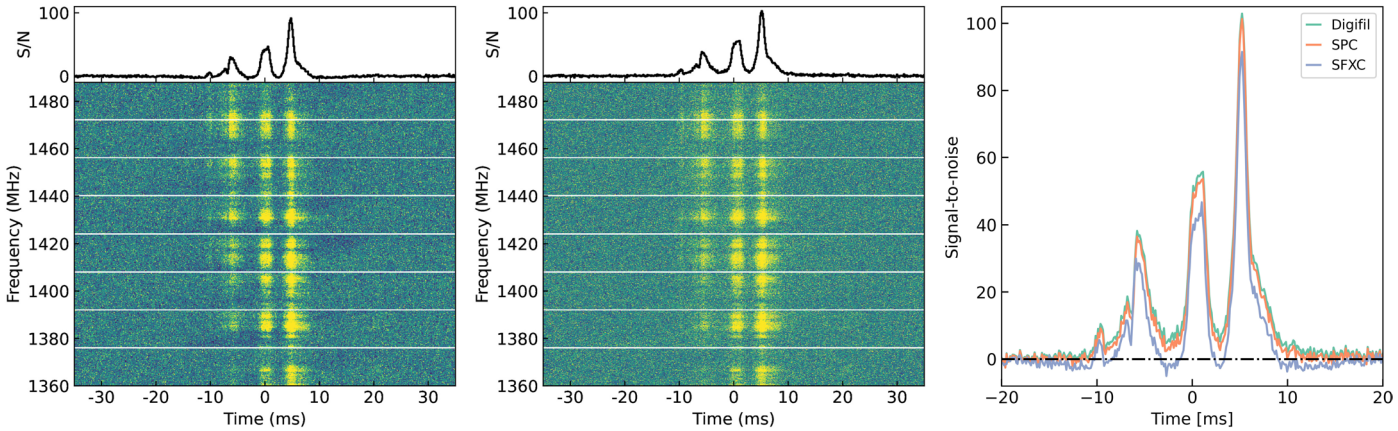

Extended Data Fig. 4 | Illustration of the effect of 2-bit sampling on the total intensity data. Here, the effect is shown for burst B08-08. Left: Processed with SFXC; the top panel shows the frequency-averaged time series while the bottom panel shows the dedispersed dynamic spectrum. The response of the system to the brightest scintillation peaks is visible as dark 'depressions' across the affected subbands (the edges of subbands are indicated by horizontal white lines). Middle: The same burst processed with digifil. The 2-bit correction removes the depression but, at the same time, overcompensates for this instrumental effect. Right: Overlay of the time series as processed with SFXC, digifil and also further processed with psrchive's SPC algorithm. While the SFXC-generated profile dips below the baseline between components, the SPC-processed version remains below the digifil time series while not reaching the zero-baseline in between components.

https://doi.org/10.1038/s41550-023-02153-z

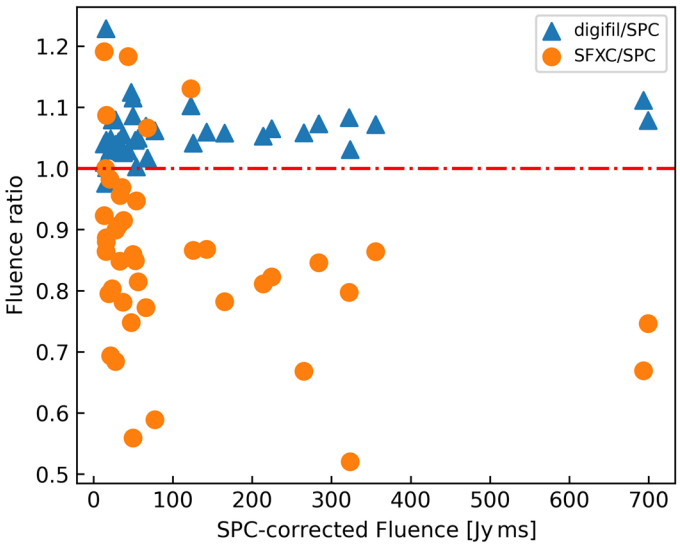

Extended Data Fig. 5 | Relative fluences computed from the SFXC- and digifil-generated filterbanks. All data points were scaled by the SPC-corrected fluences (see text for details).

https://doi.org/10.1038/s41550-023-02153-z

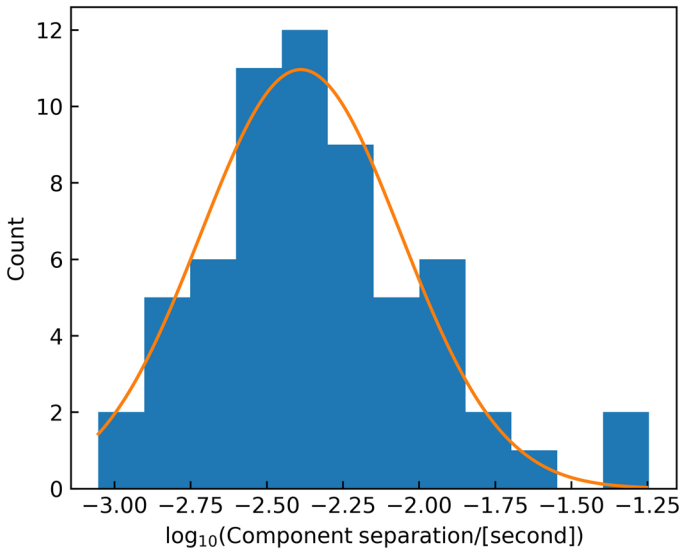

Extended Data Fig. 6 | Logarithmic distribution of wait times between burst components. The orange line is a log-normal fit that yields a characteristic wait time of $\delta t = 4.1^{+4.4}_{-2.1}$ms.

https://doi.org/10.1038/s41550-023-02153-z

Extended Data Table 1 | Expected burst numbers at P- and C-band

Spectral index	Threshold[a] [Jy ms]	MJD range 1 59305–59363			MJD range 2 59602–59641		
		L[b]	P[c]	C[c]	L[b]	P[c]	C[c]
0.0	91	4	2.1	-	6	0.6	-
	5	9	-	2.0	31	-	7.6
−1.5	10.2	9	4.8	-	31	3.2	-
	29.8	6	-	1.3	20	-	4.9

See text for details. Footnotes: [a]Detection threshold as listed in Table 1 for P- and C-band scaled to L-band using the listed spectral index. [b]Number of detected bursts at L-band. [c]Number of expected bursts given the L-band detections, the threshold, and the number of hours observed in each band.

https://doi.org/10.1038/s41550-023-02153-z

Extended Data Table 2 | Dispersion measure estimates

Burst ID	measured DM
B06-o8	411.886 ± 0.277
B08-o8	410.935 ± 0.253
B12-o8	411.189 ± 0.350
B13-o8	410.774 ± 0.286
B18-wb	411.334 ± 0.341
B19-wb	410.833 ± 0.335
B20-wb	410.621 ± 0.580
B29-wb	410.735 ± 0.558
B34-wb	411.053 ± 0.265
B42-wb	410.408 ± 0.426

These were found by running DM-phase[23] on ten bright, multi-component bursts detected throughout the campaign.

https://doi.org/10.1038/s41550-023-02153-z

Extended Data Table 3 | Burst properties

Burst ID	Station	TOA[a] [MJD]	Peak S/N[b]	Fluence[c] [Jy ms]	Number of components	Width[d] [ms]	Spectral Luminosity[e] [10^{32} erg s^{-1} Hz^{-1}]	BW[f] [MHz]	ν_s[g] [MHz]
B01-st	St	59319.513506069*	45.7	383.1 ± 76.6	1	5.24	148.83 ± 29.77	98	0.3 ± 0.3
B02-o8	O8	59326.642775092	7.6	13.3 ± 2.7	1	6.66	4.07 ± 0.81	128	0.9 ± 0.8
B03-o8	O8	59329.517962388	7.6	49.6 ± 9.9	3	28.93	3.49 ± 0.70	128	0.4 ± 0.3
B04-o8	O8	59337.453941128*	4.5	28.8 ± 5.8	1	14.85	3.95 ± 0.79	128	0.9 ± 1.7
B05-o8	O8	59337.797038104	28.5	53.8 ± 10.8	1	6.66	16.48 ± 3.30	128	0.4 ± 0.3
B06-o8	O8	59349.567736580	76.9	265.2 ± 53.0	4	19.46	27.76 ± 5.55	128	0.4 ± 0.1
B06-st	St	59349.567736521*	114.5	1593.6 ± 318.7	3	9.18	353.80 ± 70.76	98	0.2 ± 0.1
B07-o8	O8	59349.572426981	3.4	15.5 ± 3.1	1	27.39	1.15 ± 0.23	128	0.1 ± 0.5
B08-tr	Tr	59356.468854046	108.2	453.0 ± 90.6	4	23.04	40.05 ± 8.01	256	0.5 ± 0.1
B08-o8	O8	59356.468854047	137.4	693.4 ± 138.7	4	23.81	59.32 ± 11.86	128	0.2 ± 0.2
B09-o8	O8	59358.428680977	5.8	23.5 ± 4.7	1	15.36	3.11 ± 0.62	128	0.3 ± 0.5
B10-st	St	59362.433401658*	9.0	278.2 ± 55.6	3	10.05	56.39 ± 11.28	58	0.2 ± 0.2
B11-o8	O8	59485.203789751	5.2	47.5 ± 9.5	2	29.18	3.31 ± 0.66	128	0.4 ± 0.4
B12-o8	O8	59485.238856691	88.6	165.1 ± 33.0	2	17.66	19.04 ± 3.81	128	0.3 ± 0.2
B13-o8	O8	59485.970826378	76.4	322.3 ± 64.5	5	18.69	35.13 ± 7.03	128	0.6 ± 0.1
B14-o8	O8	59485.983419756	3.5	15.8 ± 3.2	1	17.41	1.85 ± 0.37	128	0.6 ± 0.4
B15-wb	Wb	59602.992809140	4.6	27.7 ± 5.5	1	15.36	3.68 ± 0.74	128	0.3 ± 0.4
B16-wb	Wb	59603.754507174	6.2	49.8 ± 10.0	1	33.02	3.07 ± 0.61	128	3.8 ± 4.2
B17-wb	Wb	59603.799227784	14.0	33.1 ± 6.6	1	5.38	12.56 ± 2.51	128	0.2 ± 0.2
B18-wb	Wb	59605.835730583	122.1	699.2 ± 139.8	3	17.15	83.03 ± 16.61	128	0.3 ± 0.1
B19-wb	Wb	59608.845447891	57.5	284.0 ± 56.8	2	15.87	36.45 ± 7.29	128	0.3 ± 0.2
B20-wb	Wb	59608.888891277	52.9	213.7 ± 42.7	3	8.70	50.02 ± 10.00	128	0.5 ± 0.1
B21-wb	Wb	59609.758499853	6.1	16.0 ± 3.2	1	5.89	5.53 ± 1.11	128	0.7 ± 0.5
B22-o8	O8	59611.690224668	17.3	67.7 ± 13.5	3	75.01	1.84 ± 0.37	256	1.4 ± 0.6
B23-wb	Wb	59611.911786572	6.5	66.0 ± 13.2	3	68.35	1.97 ± 0.39	128	0.6 ± 0.3
B24-wb	Wb	59612.971443269	14.7	37.8 ± 7.6	1	4.86	15.82 ± 3.16	128	0.3 ± 0.3
B25-o8	O8	59613.913140698	30.2	122.8 ± 24.6	8	46.59	5.37 ± 1.07	512	0.3 ± 0.1
B25-wb	Wb	59613.913141220	10.8	56.3 ± 11.3	3	19.20	5.97 ± 1.19	128	0.1 ± 0.1
B26-o8	O8	59614.043244112	10.5	14.9 ± 3.0	2	6.14	4.93 ± 0.99	512	0.4 ± 0.2
B26-wb	Wb	59614.043244218	7.4	36.9 ± 7.4	2	7.68	9.79 ± 1.96	128	0.7 ± 0.3
B27-o8	O8	59614.048814839	23.4	77.2 ± 15.4	2	16.90	9.30 ± 1.86	512	0.5 ± 0.3
B27-wb	Wb	59614.048814942	24.6	142.5 ± 28.5	3	16.90	17.18 ± 3.44	128	0.5 ± 0.2
B28-wb	Wb	59615.749713619	6.9	28.0 ± 5.6	2	8.45	6.76 ± 1.35	128	0.1 ± 0.2
B29-wb	Wb	59615.845856436	41.4	224.6 ± 44.9	2	11.78	38.86 ± 7.77	128	0.2 ± 0.1
B30-wb	Wb	59616.969495614	5.4	19.3 ± 3.9	1	6.40	6.14 ± 1.23	128	0.2 ± 0.3
B31-st	St	59618.924807243*	21.3	64.5 ± 12.9	2	9.39	13.99 ± 2.80	98	0.4 ± 0.3
B31-o8	O8	59618.924807260	55.1	51.1 ± 10.2	2	8.19	12.72 ± 2.54	512	0.4 ± 0.2
B32-st	St	59618.962324541*	9.2	57.4 ± 11.5	2	7.86	14.88 ± 2.98	98	0.3 ± 0.2
B32-o8	O8	59618.962324547	9.8	21.6 ± 4.3	1	7.94	5.54 ± 1.11	512	0.4 ± 0.2
B33-st	St	59619.730729859*	5.6	26.4 ± 5.3	1	7.43	7.24 ± 1.45	98	0.5 ± 0.6
B33-wb	Wb	59619.730730266	7.7	33.6 ± 6.7	2	7.42	9.22 ± 1.84	128	0.2 ± 0.2
B34-st	St	59619.773110130*	27.5	250.7 ± 50.1	3	12.89	39.62 ± 7.92	98	0.6 ± 0.2
B34-wb	Wb	59619.773110529	52.0	355.6 ± 71.1	3	14.85	48.78 ± 9.76	128	0.5 ± 0.2
B35-wb	Wb	59620.855108645	9.4	52.4 ± 10.5	2	7.68	13.91 ± 2.78	128	0.3 ± 0.2
B35-st	St	59620.856761425*	7.8	52.0 ± 10.4	2	8.96	11.83 ± 2.37	98	0.2 ± 0.2
B36-wb	Wb	59620.913032971	6.6	20.4 ± 4.1	2	7.42	5.59 ± 1.12	128	–[h]
B37-st	St	59622.759765600*	12.1	50.0 ± 10.0	1	10.70	9.51 ± 1.90	98	1.2 ± 0.8
B37-wb	Wb	59622.759765813	5.9	35.8 ± 7.2	1	10.75	6.79 ± 1.36	128	0.5 ± 0.2
B38-st	St	59622.795156022*	6.7	26.2 ± 5.2	2	6.99	7.62 ± 1.52	98	3.6 ± 4.1
B38-wb	Wb	59622.795156240	3.7	13.4 ± 2.7	1	8.70	3.15 ± 0.63	128	0.5 ± 0.4
B39-st	St	59622.962155172*	3.4	11.0 ± 2.2	1	4.37	5.13 ± 1.03	98	–[h]
B39-wb	Wb	59622.962155576	7.3	16.2 ± 3.2	1	6.14	5.37 ± 1.07	128	0.4 ± 0.3
B40-st	St	59624.668435558*	5.3	16.6 ± 3.3	1	4.37	7.73 ± 1.55	98	0.2 ± 0.2
B41-wb	Wb	59633.774378172	9.0	31.6 ± 6.3	2	9.22	6.99 ± 1.40	128	0.4 ± 0.2
B42-tr	Tr	59633.927686106	25.1	61.0 ± 12.2	3	11.01	11.30 ± 2.26	128	0.4 ± 0.2
B42-wb	Wb	59633.927686140	32.0	125.5 ± 25.1	2	7.68	33.28 ± 6.66	128	0.6 ± 0.1
B43-st	St	59635.821821805*	9.6	45.0 ± 9.0	1	11.58	7.92 ± 1.58	98	0.5 ± 0.3
B44-st	St	59636.618137128*	4.9	71.5 ± 14.3	6	68.38	2.13 ± 0.43	98	0.2 ± 0.2
B45-st	St	59637.952097942*	6.6	36.1 ± 7.2	2	8.74	8.42 ± 1.68	98	1.0 ± 0.4
B46-st	St	59639.813991726*	5.8	38.6 ± 7.7	2	21.85	3.60 ± 0.72	98	0.5 ± 1.0

See text for details on how the values were derived. Footnotes: [a]Time of arrival at the solar system barycenter at infinite frequency in TDB (using a DM of 410.8 pc cm^{-3}, a dispersion measure constant of 1/0.000241 GHz^{2}cm^{3}pc^{-1} μs and as (J2000) position RA=05:08:03.5, Dec=+26:03:37.8; for times marked with a *, a DM constant of 4.14880568679703 GHz^{2}cm^{3}pc^{-1}ms was used). For multi-component busts, the TOA is defined as the middle between the peak of the first and the last component. [b]The peak S/N of the brightest component. [c]Computed as the sum over the measured fluence of each component. We assume a conservative error of 20% for all bursts, dominated by the uncertainty of the SEFD. [d]Manually determined time span between start of first and end of last component. [e]Computed using D_L=453 Mpc, z=0.098 and the listed width. [f]Bandwidth used for computing the fluence. This is often the full available observing bandwidth. [g]Weighted average over the measured scintillation bandwidth per component. [h]No measurement was possible due to low S/N.